

Attractive carbon black dispersions: structural and mechanical responses to shear

Julien Bauland,¹ Louis-Vincent Bouthier,² Arnaud Poulesquen,³ and Thomas Gibaud^{1, a)}

¹⁾Univ Lyon, Ens de Lyon, CNRS, Laboratoire de Physique, 69342 Lyon, France

²⁾Groupe CFL, CEMEF, Mines Paris PSL, 1 Rue Claude Daunesse, 06904 Sophia Antipolis, France

³⁾CEA, DES, ISEC, DE2D, SEAD, LCBC, Université de Montpellier, Marcoule, France

(Dated: 18 March 2024)

The rheological behavior of colloidal dispersions is of paramount importance in a wide range of applications, including construction materials, energy storage systems and food industry products. These dispersions consistently exhibit non-Newtonian behaviors, a consequence of intricate interplays involving colloids morphology, volume fraction, and inter-particle forces. Understanding how colloids structure under flow remains a challenge, particularly in the presence of attractive forces leading to clusters formation. In this study, we adopt a synergistic approach, combining rheology with ultra small-angle X-ray scattering (USAXS), to probe the flow-induced structural transformations of attractive carbon black (CB) dispersions and their effects on the viscosity. Our key findings can be summarized as follow. First, testing different CB volume fractions, in the high shear rate hydrodynamic regime, CB particles aggregate to form fractal clusters. Their size conforms to a power law of the shear rate, $\xi_c \propto \dot{\gamma}^{-m}$, with $m \simeq 0.5$. Second, drawing insights from the fractal structure of clusters, we compute an effective volume fraction ϕ_{eff} and find that microstructural models adeptly account for the hydrodynamic stress contributions. We identify a critical shear rate $\dot{\gamma}^*$ and a critical volume fraction ϕ_{eff}^* , at which the clusters percolate to form a dynamical network. Third, we show that the apparent yield stress measured at low shear rates inherits its properties from the percolation point. Finally, through data scaling and the integration of the Einstein's viscosity equation, we revisit and discuss the Caggioni-Trappe-Spicer model, revealing a significant connection between its empirical parameters and the structural properties of CB dispersions under flow.

I. INTRODUCTION

Colloidal dispersions are encountered in numerous application fields, for instance as cement paste in construction industry¹, as drilling muds during extraction operations², as flowable electrodes used for energy storage³, or as oil in water emulsions in food industry^{4,5}. In the aforementioned examples, predicting and controlling the viscosity of the dispersions is of key importance to optimize their use. The rheological behavior of colloidal dispersions is usually non-Newtonian, and depends on the shape, volume fraction and interaction potential between the particles⁶. In scenario with low volume fractions ϕ_{r_0} and strong attractive forces, colloidal dispersions become unstable, and particles of radius r_0 aggregate into "flocs" or "clusters" of radius ξ_c . These clusters exhibit a fractal structure and the number of particles N_c in a cluster scales as⁷:

$$N_c = \left(\frac{\xi_c}{r_0} \right)^{d_f} \quad (1)$$

with d_f the fractal dimension of clusters. Because of their fractal nature, clusters cannot continue growing indefinitely as the volume they occupy increases faster than the available space. Therefore, there may come a point where the spheres enclosing the clusters reach a random close packing limit. At this limit, the spatial separation between the clusters approaches zero, allowing them to interconnect through the outermost particles on their respective surfaces⁸. This outcome

is valid at rest⁹ and under shear¹⁰. The shear-dependent structure of clusters is a crucial factor for understanding the dispersion properties, whether the dispersion is at rest or subjected to shear.

Under quiescent conditions, aggregation is driven by the thermal energy. The aggregation rate is either limited by particles diffusion¹¹ or by the reaction probability upon collision¹², leading to loosely structured clusters⁷ with $1.7 < d_f < 2.1$. When the volume fraction is sufficiently high, further aggregation of clusters leads to the formation of a space-spanning network called a "gel", that displays an elastic modulus and a yield stress¹³.

When attractive dispersions experience flow, clusters tend to condense, resulting in $d_f > 2.4$ ¹⁴⁻¹⁶. The equilibrium cluster size ξ_c is determined by the balance between the viscous drag force acting on a particle (F_{visc}) and the attractive forces holding particles together (F_{attr}). This balance is quantified by the Mason number, expressed as¹⁷:

$$\text{Mn} = \frac{F_{\text{visc}}}{F_{\text{attr}}} = \frac{6\pi\eta r_0^2 \dot{\gamma}}{U/\delta} \quad (2)$$

with r_0 (m) the particle radius, $\dot{\gamma}$ the shear rate and η a viscosity that we will define later. U (N.m) and δ (m) are the depth and width of the attractive interaction potential, respectively. An important question revolves around the nature of the viscous force involved in Eq. 2 and the stress experienced by clusters. From the dependence of the cluster size with the shear rate, it was argued that clusters are sufficiently distant, and that the fluid stress $\sigma_f = \eta_f \dot{\gamma}$ was the primary factor^{14,18} with η_f the viscosity of the background fluid. An alternative proposition suggests that interactions between clusters would lead to a substantial increase in hydrodynamic stress¹⁹ and

^{a)}Corresponding author, thomas.gibaud@ens-lyon.fr

that the dispersion viscosity η that must be taken into account in Eq. 2 to explain the equilibrium cluster size. This debate underscores the complex interplay of factors involved in cluster formation and behavior in attractive colloidal dispersions submitted to flow. The choice between the fluid stress or the dispersion stress as the key determinant might depends on the characteristics of the dispersion system and the experimental conditions. In all cases, the Mason number was effectively reported to control the cluster size at high shear^{18–20}.

Under this framework, the structuring degree of the dispersion is set by the flow, and in return the flow is affected by the structure of the dispersion. These reversible and time-dependent flow-induced structural changes are called "thixotropy"¹⁷. Macroscopically, attractive dispersions usually show two regimes, depending on the Mn value. At high Mn, the shear rate dependence of the cluster size leads to a shear thinning behavior and the clusters size was reported to scale as

$$\xi_c \propto \text{Mn}^{-m}, \quad (3)$$

where m is the breaking exponent. There are yet no consensus on the value of the breaking exponent m . Wessel and Ball²¹ first proposed that the maximum cluster size should scale with the hydrodynamic stress with $m = 1/3$. More complex models distinguish highly deformable clusters from rigid clusters, yielding $m = 1/2$ and $m = 1/3$, respectively^{22,23}. Recently, Bouthier et al.²⁰ proposed that m should vary with the fractal dimension of clusters, with $m = 1/(1 + d_f)$. Besides analytical calculations, experiments^{14,19,24,25} and simulation^{18,26} results have reported values for m ranging from 0.2 to 1. At low values of Mn, the cluster size becomes independent of the shear rate¹⁸ as clusters fill the space, forming a transient network and leading to an apparent yield stress σ_y . Varga and Swan¹⁸ proposed that percolation would occur at a critical value of the Mason number, $\text{Mn}_c \propto \phi_{r0}^{2/(3-d_f)}$ with ϕ_{r0} the volume fraction of particles.

In practice, the rheological properties of attractive dispersions are assessed by applying a given shear rate $\dot{\gamma}$ and measuring the resulting stress with $\sigma = \eta \dot{\gamma}$. To assess the dependence of the dispersions viscosity with the shear rate, a flow curve test is commonly conducted. This test consists in applying a stepwise increment in shear rate with a given step duration Δt . Due to the thixotropic nature of attractive dispersions, a finite amount of time is necessary to reach the equilibrium viscosity. Consequently, a rapid increase in shear rate will only characterize the transient viscosity. Flow curves, whether represented as σ vs $\dot{\gamma}$ or η vs $\dot{\gamma}$, are usually described using the Herschel-Bulkley model²⁷:

$$\sigma = \sigma_y \left[1 + \left(\frac{\dot{\gamma}}{\dot{\gamma}_{HB}^*} \right)^{n_{HB}} \right], \quad (4)$$

where σ_y is the yield stress (Pa), $\dot{\gamma}_{HB}^*$ a critical shear rate and n_{HB} an empirical exponent. This empirical model effectively captures both the yield stress and the shear-thinning behavior of attractive dispersions with $n_{HB} < 1$. However, it does not provides any microscopic interpretation of its parameters as it dismiss the cluster properties. In more developed models,

like structural kinetics model¹⁷, the rheological parameters of the constitutive equation are set as a function of a structural parameter λ , comprised between 0 and 1 for a totally broken or fully developed cluster structure, respectively. By introducing kinetics equation for λ , the structural kinetics models efficiently capture the time-dependent properties of dispersions, but the parameter λ cannot be easily related with any physical aspects of the microstructure. In population balanced models²⁸, a partial differential equation tracks the evolution of the size distribution function with respect to time. The equation includes terms that represent the rates of various particle interactions or transformations. Solving this equation provides insights into the evolution of the distribution of particle sizes over time and under different flow conditions.

In this study, we choose to focus on microstructural models, which directly rely on structural changes that can experimentally be measured. In such models, the shear stress is decomposed as a sum of an elastic σ_e and an hydrodynamic σ_h contribution, so that $\sigma = \sigma_e + \sigma_h$. The elastic stress originates from the network and is typically treated as a constant, derived from the particle interactions and the cluster properties^{29,30}. The hydrodynamic stress σ_h is calculated by introducing an effective volume fraction of clusters ϕ_{eff} . ϕ_{eff} is the equivalent volume fraction of spheres, considering the fractal structure of clusters^{29–31}:

$$\phi_{\text{eff}} = \frac{\phi_{r0}}{k} \left(\frac{\xi_c}{r_0} \right)^{3-d_f} \quad (5)$$

where ϕ_{r0} is the volume fraction of primary particles and k is a scaling constant usually approximated as unity. Then, various models have been used to relate ϕ_{eff} with the viscosity of the dispersion η ^{17,32–34}. Assuming that the viscosity dependence on the volume fraction follows the one of a hard sphere dispersion, a generalized viscosity equation for concentrated regimes can be used,^{35,36} such as the one proposed by Krieger and Dougherty³⁷:

$$\eta = \eta_f \left(1 - \frac{\phi_{\text{eff}}}{\phi_{\text{eff}}^M} \right)^{-2.5\phi_{\text{eff}}^M} \quad (6)$$

with ϕ_{eff}^M the maximum packing fraction of hard spheres, typically $\phi_{\text{eff}}^M \simeq 0.64$.

In summary, a significant body of work aimed to establish connections between the cluster properties and the viscosity of colloidal dispersions. However, few studies have probed both aspects simultaneously and structural characterizations are lacking. Consequently, the validity of microstructural models has not been thoroughly tested¹⁷ and some questions have still to be answered: How the cluster properties change with shear rate? Are cluster properties driven by stress or shear rate? Is the decomposition of the stress into an elastic and hydrodynamic contribution sufficient to model a flow curve?

To address these questions, we follow an experimental approach with carbon black (CB) dispersions in oil, chosen as study model. Such dispersions present peculiar and fundamental rheological properties^{38–40} including rheopexy^{41–43},

delayed yielding^{44,45}, fatigue^{46,47}, rheo-conductive properties⁴⁸, sensitivity to flow cessations^{49,50} and rheo-acoustic properties^{51,52}. Furthermore, CB dispersions directly find utility in numerous applications such as ink⁵³, cement⁵⁴ or semi-solid flow batteries⁵⁵.

The paper is structured as follows. We initially characterize the flow properties of CB dispersions using rheology across a range of volume fractions spanning from 0.6% to 4.1%. Then, we examine the structural features of these dispersions under flow conditions using ultra small-angle X-ray scattering (USAXS)⁵⁶. Finally, we establish a relationship between the shear-dependent viscosity of the dispersions and their structural parameters by employing microstructural models.

II. MATERIAL AND METHODS

A. Carbon black dispersions

CB particles (Vulcan®PF, Cabot, density $d_{cb} = 2.26 \pm 0.03$) were dispersed in mineral oil (RTM17 Mineral Oil Rotational Viscometer Standard, Paragon Scientific, viscosity $\eta_f = 252.1$ mPa.s at $T = 25^\circ\text{C}$, density $d_{oil} = 0.871$) at mass fractions c_w ranging from 1.5 to 10 % (w/w)⁴⁹. The corresponding volume fractions of CB particles ϕ_{r_0} were calculated as $\phi_{r_0} = c_w / \left(c_w + \frac{d_{cb}}{d_{oil}} (1 - c_w) \right)$. After mixing, dispersions were sonicated during 2h in an ultrasonic bath (Ultrasonic cleaner, DK Sonic®, United-Kingdom) to ensure that all particles were fully dispersed.

B. Rheology

Experiments were carried out with two stress controlled rheometers: (i) a Haake RS6000 (Thermo Scientific) and (ii) a MCR 301 (Anton Paar), both equipped with a Couette geometry composed of concentric polycarbonate cylinders (inner diameter 20 mm, outer diameter 22 mm and height 40 mm).

All rheological measurements were performed at 25°C . After loading the CB dispersion, a preshear, $\dot{\gamma} = 1000 \text{ s}^{-1}$, was first applied during 60 s to erase any shear history. Then, a flow curve test was performed by ramping downward from $\dot{\gamma} = 1000$ to 0.01 s^{-1} (10 pts per decade) with a duration $\Delta t = 1 \text{ s/pts}$ and measuring the resulting stress σ . A downward ramping of the shear rate was chosen to prevent heterogeneous flows (*e.g.* shear banding) usually observed for yield stress fluids in the vicinity of the yield stress⁵⁷. We varied Δt and probed 50 and 100 s/pts and found that the flow curves were identical down to $\dot{\gamma} \sim 1 \text{ s}^{-1}$ (see Appendix, Fig. 6). For shear rates $\dot{\gamma} > 1 \text{ s}^{-1}$ a stationary regime is rapidly found as observed in⁴⁹. Below $\dot{\gamma} \sim 1 \text{ s}^{-1}$, the rheology is not stationary and wall slip, sedimentation⁴³ or shear banding⁴⁴ may occur. It is noteworthy that Hipp et al.¹⁹ also performed flow curve tests on CB dispersions. However, they constructed "self-similar flow curves" through a series of rheological measurements that differ from a continuous ramping of the shear rate as performed here. Consequently, the shear history undergone

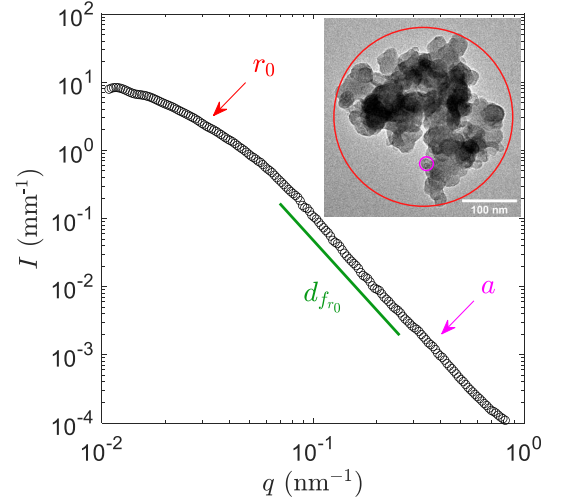


FIG. 1. Form factor of carbon black particles measured by USAXS for $\phi_{r_0} = 10^{-4}$. Carbon black particles are composed of nodules of radius a that are fused to form primary aggregates of radius r_0 and fractal dimension d_{fr_0} . Inset displays a representative electron microscopy image of a single CB particle. See Fig. 8 in Appendix for a detailed analysis of the form factor.

by the CB dispersions before each shear rate is significantly different.

C. Ultra Small angle X-ray scattering (USAXS)

The microstructural characteristics of the CB dispersion were probed using rheo-USAXS measurements conducted at the ID02 beamline within the European Synchrotron Radiation Facility (ESRF) in Grenoble, France⁵⁹. The incident X-ray beam, with a wavelength of 0.1 nm, was collimated to dimensions of $50 \mu\text{m}$ vertically and $100 \mu\text{m}$ horizontally. Utilizing an Eiger2 4M pixel array detector, two-dimensional scattering patterns were acquired. The subsequent data reduction process is detailed in⁵⁶. The scattering intensity $I(q)$ was derived by subtracting the two-dimensional scattering profiles of the carbon black dispersions and the mineral oil. Importantly, the resulting scattering intensity remained isotropic throughout this study (see Appendix, Fig. 9) and an azimuthal average was performed to obtain a one-dimensional $I(q)$. Measurements were conducted in both radial and tangential configurations, yielding equivalent results due to the isotropic nature of the dispersions microstructure over the tested q -range.

D. Transmission electron microscopy

A diluted dispersion of CB in absolute ethanol ($c_w \approx 2 \cdot 10^{-5}$) was prepared and $5 \mu\text{L}$ were deposited on a carbon grid (Carbon Film CF300-Cu, Electron Microscopy Science, England) and left to dry in a dust free environment. Individual CB particles were then imaged by transmission electron

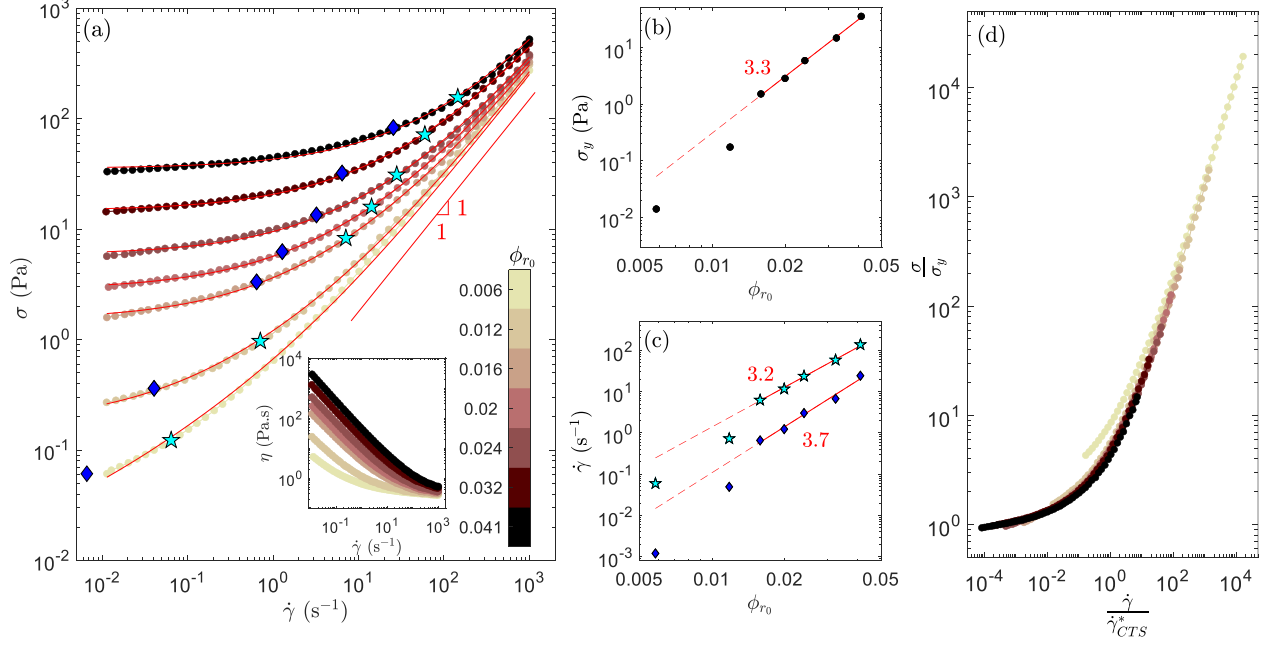


FIG. 2. Flow curve of carbon black (CB) dispersions and the Cagioni-Trappe-Spicer (CTS) model⁵⁸. (a) Shear stress σ vs shear rate $\dot{\gamma}$ during fast flow curves of CB dispersions at various volume fractions ϕ_{r0} . The red curves correspond to the best fits with the CTS model (eq. 7). Inset: viscosity η vs $\dot{\gamma}$. Evolution of the parameters of the CTS model with ϕ_{r0} : (b) Apparent yield stress σ_y ; (c) Critical shear rates $\dot{\gamma}_{CTS}^*$ (blue diamonds) and $\dot{\gamma}_{CTS}^p$ (cyan stars). $\dot{\gamma}_{CTS}^p$ is a "plastic" shear rate and $\dot{\gamma}_{CTS}^*$ is another critical shear rate obtained as $\dot{\gamma}_{CTS}^* = \sigma_y/\eta_0$, with η_0 the high shear viscosity. Red dash lines are the best power law fit of the data. (d) Normalized flow curves: σ/σ_y vs $\dot{\gamma}/\dot{\gamma}_{CTS}^*$.

microscopy (TEM) using a JEOL JEM 1400 microscope. A representative set of CB particle images is displayed in Fig. 8 in Appendix.

E. Characterization of carbon black particles

The CB particles were analyzed using TEM and USAXS. As shown in the TEM images in inset of Fig. 1, CB particles are composed of nodules of radius a that are fused to form primary aggregates of radius r_0 ⁶⁰. These two length scales, $q_{r_0} \approx 5.10^{-2}$ and $q_a \approx 4.10^{-1}$ nm $^{-1}$ are also identified on the form factor of the CB particles, measured on a diluted sample ($\phi_{r0} = 10^{-4}$) at rest (Fig. 1). The power law scaling $I(q) \propto q^{d_{fr_0}}$ at intermediate q is related to the fractal dimension of the primary aggregates d_{fr_0} . Having tested different models to fit the USAXS data (see Fig. 8 in Appendix), we estimate $a \simeq 20$ nm, $r_0 \simeq 85$ nm and $d_{fr_0} \simeq 2.8$. Vulcan PF particles are therefore small and compact aggregates in comparison with other CB particles previously reported (e.g. $r_0 \simeq 180$ nm for Vulcan XC-72^{48,52}). We note that the flow does not impact the integrity of CB particles, as evidence in Fig. 3a-b, where $I(q)$ remains constant for $5.10^{-2} < q < 2.10^{-1}$ nm $^{-1}$.

III. RESULTS AND DISCUSSION

A. Rheological properties of carbon black dispersions

We first examine the influence of the particles volume fraction ϕ_{r0} on the flow behavior of the CB dispersions. Fig. 2a displays the flow curves for dispersions with ϕ_{r0} ranging from 0.6 to 4.1%. In Fig. 2a, the flow curve exhibits a similar trend for all the tested volume fractions: a shear-thinning behavior at high shear rates and the presence of a dynamic yield stress σ_y at low shear rates. The dynamic yield stress σ_y increases with ϕ_{r0} (Fig. 2b) and its existence can even be debated at the lowest volume fraction ($\phi_{r0} = 0.006$). Dynamic oscillatory shear experiments indicate that the minimum particle volume fraction required to form a gel is $\phi_{r0}^{gel} \approx 0.01$, a value consistent across different pre-shear histories (data not presented).

To quantitatively assess the impact of ϕ_{r0} on the flow curves, two empirical models were employed: the Herschel-Bulkley²⁷ model and the Cagioni-Trappe-Spicer model⁵⁸. The Herschel-Bulkley model fit is not entirely satisfactory, especially for $\dot{\gamma} < 1$ s $^{-1}$ (see Appendix, Fig. 7). Improved fits are obtained with the Cagioni-Trappe-Spicer model (CTS)⁵⁸:

$$\sigma = \sigma_y + \sigma_y \left(\frac{\dot{\gamma}}{\dot{\gamma}_{CTS}^p} \right)^{\frac{1}{2}} + \eta_0 \dot{\gamma} \quad (7)$$

where σ_y is the yield stress (Pa), $\dot{\gamma}_{CTS}^p$ a critical shear rate

(s^{-1}) and η_0 a viscosity (Pa.s). In addition to taking into account the elastic component represented by the yield stress σ_y , this model incorporates a Newtonian viscous stress at high shear rates, $\eta_0\dot{\gamma}$. Furthermore, it introduces a "plastic" dissipation mechanism, where the stress scales with the square root of the shear rate, serving as an intermediate regime between the purely viscous and purely elastic behaviors. The elastic and plastic regimes are separated by a critical shear rate $\dot{\gamma}_{CTS}^p$. A second critical shear rates $\dot{\gamma}_{CTS}^*$ can be obtained as $\dot{\gamma}_{CTS}^* = \sigma_y/\eta_0$. It corresponds to the point at which the stress contribution of the high shear viscosity equals the yield stress.⁵⁸ In Eq. 7, the high shear viscosity η_0 can be calculated with the Einstein's viscosity⁶¹ $\eta_0 = \eta_f(1 + 2.5\phi_{r_0})$, given that both the fluid viscosity η_f and ϕ_{r_0} are known. This approximation is reasonable since all the values of ϕ_{r_0} under consideration remain low.

The CTS model yields a satisfactory fit with only two adjustable parameters, namely σ_y and $\dot{\gamma}_{CTS}^p$, displayed as function of ϕ_{r_0} in Fig 2b-c. In the case of gelling dispersions (*i.e.* $\phi_{r_0} > \phi_{r_0}^{gel}$), the yield stress follows a scaling law $\sigma_y \propto \phi_{r_0}^{3.3}$, consistent with findings in other colloidal gel systems⁶². $\dot{\gamma}_{CTS}^*$ roughly follows the same power law, $\dot{\gamma}_{CTS}^* \propto \phi_{r_0}^{3.2}$. Using σ_y and $\dot{\gamma}_{CTS}^*$ as scaling factors for the y - and x -axes, the flow curves can be rescaled onto a single master curve (Fig. 2e), provided that $\phi_{r_0} > \phi_{r_0}^{gel}$. This master curve implies a consistent microstructural scenario along the entire flow curve for all volume fractions. Furthermore, the observed relationships $\sigma_y \sim \dot{\gamma}_{CTS}^* \sim \phi_{r_0}^3$ indicates that the initial volume fraction of CB particles completely accounts for both the horizontal and vertical shifts of the flow curves as the volume fraction varies. This is noteworthy given the structural complexity expected for attractive dispersions. In the next section, our objective is to characterize the structure of CB dispersions and to provide insights into how ϕ_{r_0} influences the flow characteristics of these dispersions.

B. Microstructure of the carbon black dispersions under shear

The structural analysis of CB dispersions was conducted using USAXS at three volume fractions, namely $\phi_{r_0} = 0.6$, 1.2 and 3.2%. We recorded the scattering intensity $I(q)$ as function of the scattering wave number q within the range of 1.10^{-3} to $2.10^{-1} \text{ nm}^{-1}$ during flow curve measurements. It is noteworthy that $I(q)$ exhibited isotropic behavior for all measurements (see Appendix, Fig.9), ruling out any anisotropic structuring over the probed length scales. This isotropic behavior aligns with previous observations in CB dispersions^{19,49}. Consequently, our analysis focuses on the azimuthally averaged intensity $I(q)$.

Fig. 3a presents $I(q)$ at various shear rate values for $\phi_{r_0} = 0.032$. Similar scattering patterns were observed for dispersions at lower volume fractions, and they displayed the same shear rate dependence (see Appendix, Fig. 10). Upon transitioning from high to low shear rates, the scattering curves exhibit two and then three distinct bumps. These features become more pronounced in the Kratky representation ($I(q)q^2$

vs q), where the bumps are transformed into peaks (Fig. 3b). At higher q values (*i.e.* $q \approx 5.10^{-2} \text{ nm}^{-1}$), the first bump corresponds to the form factor of the CB particles of size r_0 , as evidenced in Fig.1. Notably, the position of this bump is independent of the shear rate as shear does not alter the size of the CB particles.

As previously stated, the scattering curves exhibit two characteristic lengths at high shear rates, denoted as r_0 and ξ_c (Fig. 3c-d), and an intermediate length scale ξ_s becomes apparent at lower shear rates (approximately $\dot{\gamma} < 75 \text{ s}^{-1}$). For a precise and empirical determination ξ_c and ξ_s and their relationship with $\dot{\gamma}$, we conducted fitting procedures on the peaks observed in the Kratky representation (Fig. 3c-d). These fittings were carried out using a log-normal function⁶³:

$$G_i(q) = \frac{A_i}{\sqrt{2\pi}\sigma_i q} \exp\left(-\frac{\ln(\frac{q}{q_i})^2}{2\sigma_i^2}\right) \quad (8)$$

where $G_i(q)$ describes a log-normal function of average position q_i , width σ_i and amplitude A_i . The estimated radius ($\xi_i = \pi/q_i$) are displayed for $\phi_{r_0} = 0.006$, 0.012 and 0.032 in Fig. 14b in Appendix.

The shear-dependent size ξ_c is attributed to the form factor of clusters, formed through the aggregation of CB particles, consistent with previous reports on CB dispersions^{19,48,49}. At high shear rates, typically $\dot{\gamma} = 800 \text{ s}^{-1}$, the lack of structure factor at low q indicates that these clusters are independent from each other (Fig. 3a-b and Fig. 10 in Appendix). Let us first focus on $\phi_{r_0} = 0.032$. At high shear rates, ξ_c is inversely proportional to the shear rate according to $\xi_c = B\dot{\gamma}^{-m}$, where $B \simeq 10^4 \text{ nm/s}^m$ and $m \simeq 0.44$ (inset of Fig. 3e). Below a critical shear rate of about 50 s^{-1} , ξ_c becomes constant with a critical value close to $2 \mu\text{m}$. This behavior coincides well with the simulation of Varga et al.¹⁸ where a similar scaling with $\dot{\gamma}$ and $m = 1/2$ was found. The evolution of ξ_c at lower volume fractions ($\phi_{r_0} = 0.006$ and 0.012) is similar to the one observed at $\phi_{r_0} = 0.032$. At high shear rates, the data even superimpose. However, at lower shear rates, data are lacking because the peak in $I(q)$ corresponding to ξ_c shifts to values lower than the minimum q accessible in the USAXS experiments. Based on simulations studies¹⁸, for $\phi_{r_0} = 0.006$ and 0.012, one can expect that the scaling $\xi_c = A\dot{\gamma}^{-m}$ holds down to a critical shear rate lower than 50 s^{-1} and that the cluster size converges to values much larger than $2 \mu\text{m}$. For $\phi_{r_0} = 0.006$ and 0.012, extrapolations of ξ_c vs $\dot{\gamma}$ (Fig. 3e) will be justified during the microstructural analysis developed in the next section.

So far, the present results show that the cluster size is governed by the background fluid stress, $\sigma_f = \eta_f\dot{\gamma}$ in agreement with^{14,18}. This is in contrast to the proposition in^{19,50}, where the dispersion stress was proposed as the determining factor (see Appendix, Fig. 12 for an evolution of ξ_c vs σ).

ξ_s is found to be independent of the shear rate and slightly diminishes as ϕ_{r_0} increases (see Appendix, Fig.14). The exact interpretation of ξ_s remains uncertain. In the context of CB gels at rest, ξ_s had previously been considered either as the separation distance between two neighboring clusters,

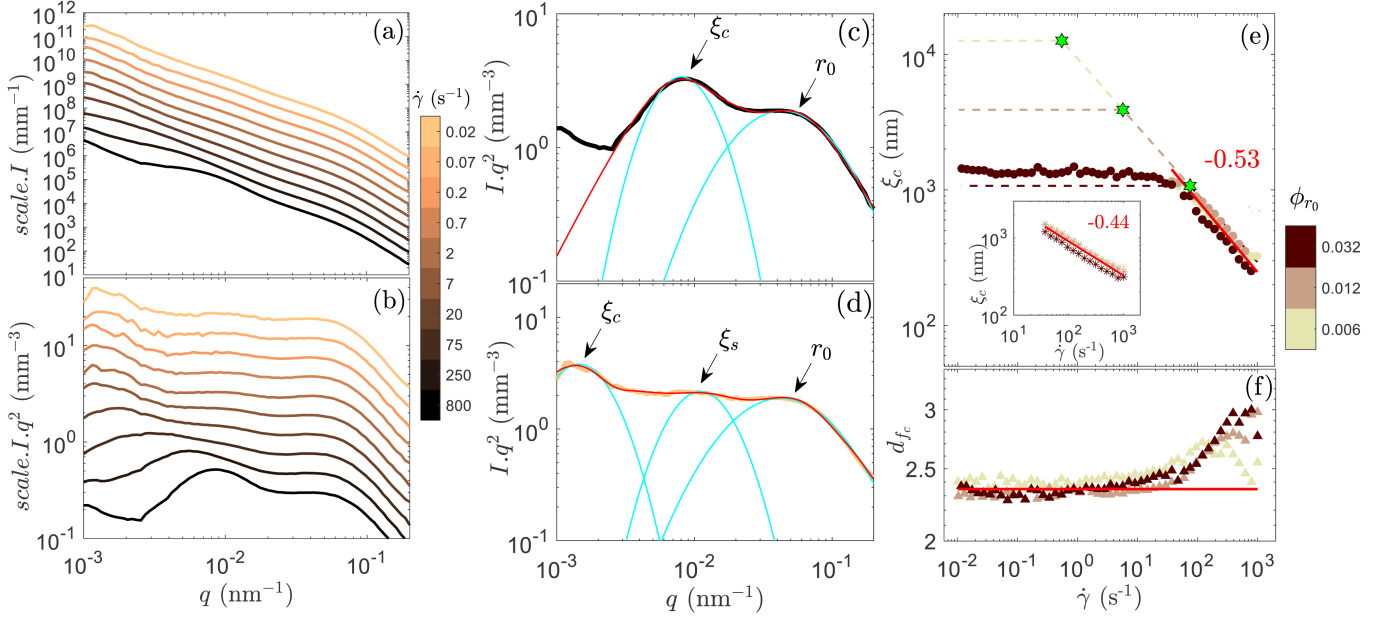


FIG. 3. Structure of the carbon black dispersion at $\phi_{r0} = 0.032$ during a flow curve test. (a) Scattered intensity $I(q)$ vs the wave vector q . (b) Kratky representation, Iq^2 vs q , of the data in (a). The curves are shifted along the y-axis for better visualization. (c)-(d) Typical scattering curves in Kratky representation obtained at high ($\dot{\gamma} = 800$ s $^{-1}$) and low shear ($\dot{\gamma} = 0.02$ s $^{-1}$), respectively. The cyan lines show the fit of the peak positions using Eq. 8. The red lines are the modified Beaucage fits using Eq. 10. (e) Evolution of the cluster size ξ_c with the shear rate $\dot{\gamma}$ for three different ϕ_{r0} , determined with the Beaucage model (Eq. 10). Note that for $\phi_{r0} = 0.006$ and 0.012 , the cluster size increases beyond the resolution of the USAXS experiments at low $\dot{\gamma}$. Dash lines are extrapolated cluster sizes and green stars correspond to the cluster size at percolation ξ_c^* , determined using the microstructural model (See Fig. 4). Red line is the best power law fit for $5 \cdot 10^2 < \dot{\gamma} < 10^3$ s $^{-1}$. Inset: ξ_c vs $\dot{\gamma}$ determined with the model-free analysis (Eq. 8). (f) Fractal dimension of the cluster d_f obtained from the modified Beaucage fit. The red line indicates $d_f = 2.35$, the mean value of d_f for $10^{-2} < \dot{\gamma} < 10^1$ s $^{-1}$.

with the idea that clusters interpenetrate due to the fact that $\xi_c > \xi_s$ ⁴⁹, or as an intermediate cluster size contributing to the construction of clusters with a size of ξ_c ⁶⁴. Alternatively, as proposed in the context of colloidal gelation under quiescent conditions, ξ_s could represent the distance over which particles are transported to the growing cluster. In this case, ξ_s is attributed to a correlation hole corresponding to the size of the depleted region surrounding the clusters^{65,66}. Given that ξ_s is smaller than ξ_c , it could also represent the depletion at the aggregation length scale.

To extract the fractal dimension of clusters, the scattering data were fitted with a modified two-level Beaucage model^{49,67}, accounting for the scattering of the particles r_0 and of the clusters ξ_c (see Appendix, section E). To account for the intermediate level ξ_s , the cluster-level term was multiplied by an empirical structure factor to account for some correlated region⁶⁷. The modified Beaucage model provides a good fit of the experimental data for all volume fractions (Fig. 3c-d and Fig. 10 in Appendix). Fig. 3e-f display the cluster sizes and fractal dimensions as function of the shear rate. The cluster sizes obtained from the modified Beaucage model correspond well with the values obtained from the model free analysis, also displayed in Fig. 3e. The power law fit of ξ_c vs $\dot{\gamma}$ yields $m \simeq 0.53$, confirming that the value of the breaking exponent is about 0.5. In Fig. 3f, the fractal dimension shows

a non-monotonic evolution with the shear rate. Overall, d_f is close to 3 at high shear rates and tends toward a constant value $d_f = 2.35$ when $\dot{\gamma}$ decreases. Determining d_f at high shear rates presents notable challenges for two primary reasons. First, in $I(q)$ vs. q , d_f is determined by the power-law relationship $I(q) \sim q^{-d_f}$ observed between the bumps associated with r_0 and ξ_c . At high shear rates, where r_0 and ξ_c are in close proximity, this power-law behavior extends over a relatively limited range, resulting in insufficient statistical data for accurate determination of d_f . Secondly, when examining the structure factor (see Appendix, Fig. 13), an anticorrelation peak is observed at $q \approx 0.03$ nm $^{-1}$ resulting from attractive interactions among the CB particles. This anticorrelation peak is not accounted by the modified Beaucage model, which leads to an overestimation of d_f . At low shear rate, the extended distance between the bumps associated to r_0 and to ξ_c allows for a more reliable determination of d_f . Moving forward, we disregards the values of d_f obtained at high shear. The fractal dimension is assumed to remain constant and equal to $d_f = 2.35$ for all ϕ_{r0} and across the entire range of shear rates ($10^{-2} < \dot{\gamma} < 10^3$ s $^{-1}$), a value which aligns with values predicted by theoretical models^{15,68} and those obtained through other experimental determinations^{14,19}.

Because of the complexity of the SAXS data, the structural analysis proposed here contains many simplifications.

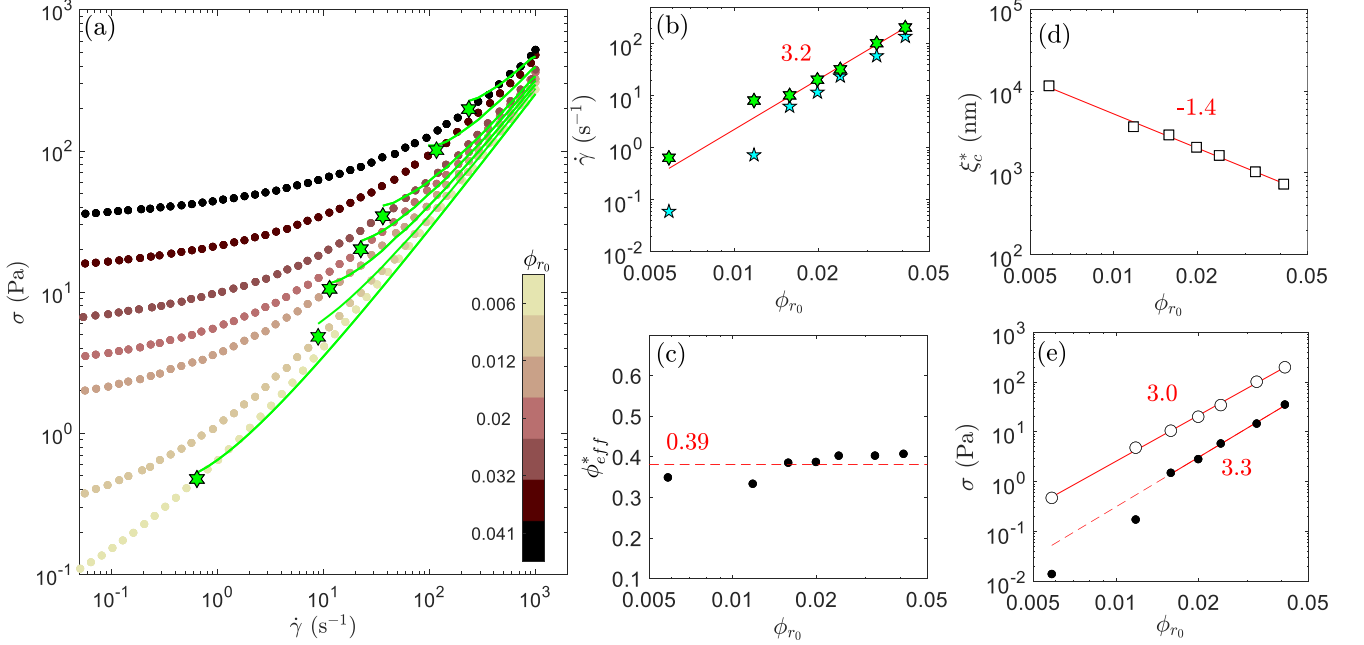


FIG. 4. Microstructural modeling of the hydrodynamic stress of the flow curve. (a) Comparison between the experimental flow curves (circles) and σ_h (green line) determined using Eq. 5 and 6 and the structural parameters of CB dispersions measured by USAXS. Stars are points of coordinate $(\dot{\gamma}^*, \sigma^*)$ such that $\sigma_h \approx \sigma$, interpreted as the dynamic percolation of clusters. (b) Comparison between $\dot{\gamma}^*$ (green hexagrams) and $\dot{\gamma}_{CTS}^*$ (cyan pentagrams) as a function of the volume fraction of CB particles ϕ_{r0} . (c) Effective volume fraction of clusters at percolation ϕ_{eff}^* displayed as function of ϕ_{r0} . Dash line indicates the mean value of $\phi_{eff}^* \approx 0.39$. (d) Cluster length ξ_c^* at percolation displayed as a function of ϕ_{r0} . Red line indicates the best power fit. (e) Comparison between the stress at percolation σ^* (empty circles) and the apparent yields stress σ_y (solid circles) as a function of ϕ_{r0} . Red line indicates the best power law fit.

Nonetheless, from this approach, we have extracted the general trend of the structuring of CB dispersions under flow: the cluster size is a function of the shear rate so that $\xi_c \propto \dot{\gamma}^{-m}$ with m approximated to 0.5, and the fractal dimension of clusters is considered to be constant with $d_f = 2.35$. The analysis developed thereafter relies on this approximations and suffice to model the flow curves.

C. Modeling the hydrodynamic regime of the flow curve based on the cluster structure.

In the previous section, rheo-USAXS measurements have shown that CB dispersions undergo an hydrodynamic regime at high shear rates. In this regime, for all ϕ_{r0} , the cluster size scales as $\xi_c \propto \dot{\gamma}^{-m}$ with $m \approx 0.5$ and their fractal dimension remains constant at $d_f \approx 2.35$. For the lowest volume fractions, due to experimental limitations, the cluster size cannot be measured beyond 2 μm and the extent of the hydrodynamic regime is not directly accessible. To address this limitation, the cluster size is extrapolated based on the relationship $\xi_c \propto \dot{\gamma}^{-m}$ observed in Fig. 3e. Using the measured and extrapolated microstructural parameters of the CB dispersions, an hydrodynamic stress $\sigma_h = \eta(\phi_{eff})/\dot{\gamma}$ is calculated using Eq. 5

for ϕ_{eff} and Eq. 6 for η . The scaling factor k in Eq. 5 was calculated⁶⁹ as $k \approx 4.46d_f^{-2.08}$ leading to $k \approx 0.75$.

As reported in Fig. 4a, σ_h captures well the flow curves down to a critical shear rate $\dot{\gamma}^*$, identified when σ_h becomes larger than the dispersion stress σ . Indeed, extrapolation of the cluster size ξ_c leads to an increase of σ_h up to $\sigma_h \geq \sigma$. This point is interpreted as a percolation point where the cluster growth becomes restricted by percolation into a dynamic network, with an effective volume fraction ϕ_{eff}^* and an effective yield stress σ^* . Consequently, for $\dot{\gamma} \leq \dot{\gamma}^*$, the cluster size is assumed to become constant and equals at ξ_c^* , as depicted in Fig. 3e where $\dot{\gamma}^*$ is pointed out by stars. This analysis is consistent with the scattering data at $\phi_{r0} = 0.032$, where the cluster sizes at low shear rates are available. Fig. 5b displays the dispersion viscosity η vs ϕ_{eff} , the effective volume fraction of clusters. The collapse of viscosity onto a master curve confirms that the rheology of the CB dispersions depends on the shear dependent volume fraction of clusters. The Krieger-Dougherty fit (red line) accurately describes the dispersions behavior up to approximately $\phi_{eff}^* \approx 0.4$, which sets the upper limit in effective volume fraction of the hydrodynamic regime.

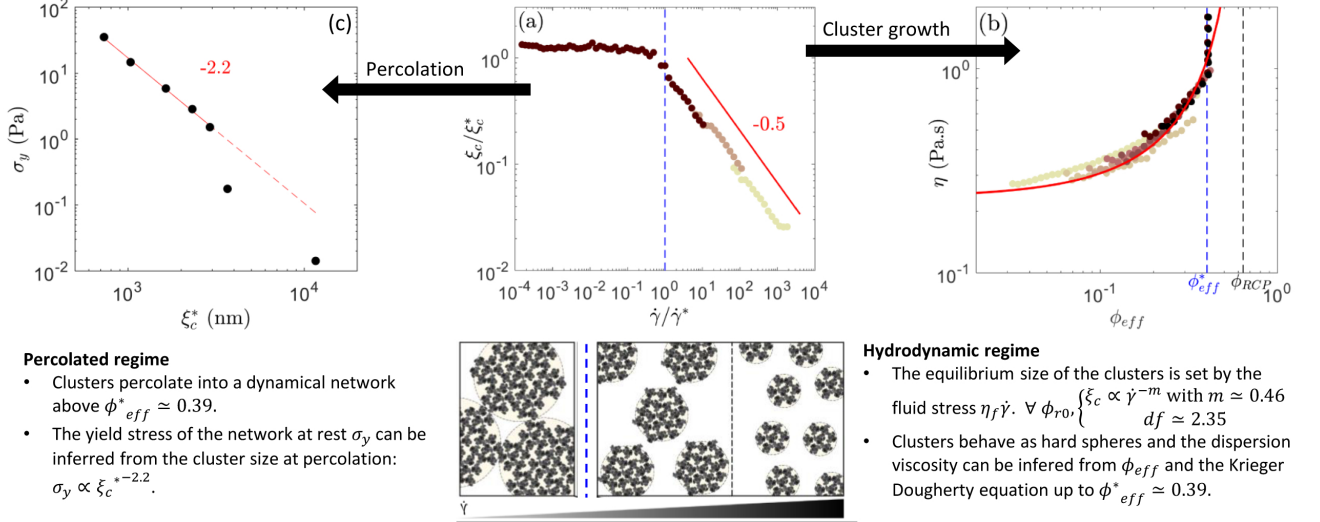


FIG. 5. Transition between the hydrodynamic regime and dynamic percolation. (a) Normalized cluster size ξ_c/ξ_c^* as a function of the normalized shear rate $\dot{\gamma}/\dot{\gamma}^*$. ξ_c^* and $\dot{\gamma}^*$ are the cluster size and shear rate at percolation, respectively. (b) Viscosity η of the CB dispersions as a function of the effective volume fraction of clusters ϕ_{eff} using Eq. 5. The red line is the viscosity issued from the Krieger-Dougherty model with $\eta_f = 0.234$ Pa.s and $\phi_{eff}^M = 0.64$. Blue and black dotted lines indicate the volume fraction of clusters at percolation ϕ_{eff}^* and at ϕ_{eff}^M , respectively. (c) Yield stress σ_y as a function of the cluster size at percolation ξ_c^* for dispersions with different volume fractions of carbon black particles. The red line represents the best-fitting power law. Bottom: Schematic of the evolution of the CB dispersions microstructure with the shear rate $\dot{\gamma}$.

D. Properties of the percolation point ($\dot{\gamma}^*$, σ^*).

The values of $\dot{\gamma}^*$, ξ_c^* , σ^* and ϕ_{eff}^* are plotted as function of ϕ_{r0} in Fig. 4b-e. As mentioned in the previous section, these parameters relate of the structure of dispersions when clusters are assumed to percolate into a dynamic network.

In Fig. 4b, $\dot{\gamma}^*$, obtained from the microstructural approach and $\dot{\gamma}_{CTS}^*$, obtained from the CTS model, are overlaid for $\phi_{r0} > \phi_{r0}^{gel}$. Thus, $\dot{\gamma}_{CTS}^*$, used to rescale the flow curves in Fig. 2, is now identified as the shear rate at which clusters percolate. In Fig. 4c, $\phi_{eff}^* \approx 0.39$ is constant for all ϕ_{r0} . This value is lower than the random close packing fraction of hard spheres, as illustrated on Fig. 5. Percolation below random close packing has been previously reported for non-Brownian dispersions with adhesive constraints at an "adhesive close packing" fraction $\phi_{acp} = 0.55^{70}$. Varga et al.¹⁸ have proposed that a critical Mn value for a percolated network could be obtained as $Mn_c \propto \phi_{r0}^{2/(3-d_f)}$. Assuming that $Mn \propto \dot{\gamma}$, the critical shear rate $\dot{\gamma}^*$ should scale with ϕ_{r0} with a power exponent $2/(3 - d_f) \simeq 3.1$ given that $d_f = 2.35$. This is consistent with the observed scaling $\dot{\gamma}^* \propto \phi_{r0}^{3.2}$ observed in Fig. 4b.

As shown in Fig. 4d, the cluster size at percolation ξ_c^* decreases with ϕ_{r0} as ϕ_{eff}^* is reached at higher shear for the highest volume fractions. In fractal aggregation theories^{71,72}, it is assumed that the gel network is built of closely packed clusters at $\phi_{eff}^* = 1$ which directly yields $\xi_c \propto \phi_{r0}^{1/(d_f-3)}$. For CB dispersions, $\phi_{eff}^* \neq 1$ but ϕ_{eff}^* is constant and the observed scaling $\xi_c^* \propto \phi_{r0}^{-1.4}$ aligns well with $1/(d_f - 3) \approx -1.5$ given that $d_f = 2.35$ (Fig. 4d). Fig. 4e compares the dependency of σ_y , measured in the zero shear rate limit, and σ^* on ϕ_{r0} .

Interestingly, both quantities exhibit a similar scaling pattern with respect to ϕ_{r0} . This observation supports the idea that the value of σ_y is a direct outcome of the percolation point. Indeed, when σ_y is plotted against ξ_c^* (Fig. 5(c)), it is found that $\sigma_y \propto \xi_c^{*-2.2}$ a close match to what one would expect²⁰: $\sigma_y \propto \xi_c^{-2}$ for a network of characteristic size ξ_c . It is worth mentioning that, when the measuring time Δt of the flow curve increases (see Fig. 6 in Appendix), this direct dependence between σ_y and ξ_c^* is probably lost as structural rearrangements may occur at low shear rates.

To sum up, in Fig. 2 the flow curve σ vs $\dot{\gamma}$ of CB dispersions at various ϕ_{r0} have been rescaled using a critical shear rate $\dot{\gamma}_{CTS}^*$ and σ_y as scaling factors for the x- and y-axis, respectively. Now, the origin of this scaling can be understood on a microstructural basis. The critical shear rate $\dot{\gamma}_{CTS}^*$ corresponds to the dynamic percolation of clusters at $\phi_{eff}^* \simeq 0.39$. The decrease of the cluster size ξ_c^* at percolation is then responsible for the increase of σ_y with ϕ_{r0} , as the network structure in the zero shear limit is inherited from the percolation point. When ϕ_{r0} approaches ϕ_{r0}^{gel} , dispersions no longer display a yield stress and the structuring at low shear is somewhat different. The percolation point, defined by $\dot{\gamma}^*$, ξ_c^* , σ^* , and ϕ_{eff}^* , holds significant importance in understanding the flow behavior of CB particles, being the transition point between the hydrodynamic regime and the dynamic percolation of clusters. In Fig. 5a, ξ_c vs $\dot{\gamma}$ at various ϕ_{r0} can be normalized onto a master curve using the percolation point coordinates, i.e. $\dot{\gamma}^*$ and ξ_c^* , as scaling factors for the x- and y-axis, respectively. The experimental results displayed on Fig. 5a are fully consistent with simulations performed in¹⁸.

IV. CONCLUSION AND PERSPECTIVES

A series of rheo-USAXS experiments was conducted on CB dispersions with $\phi_{r0} \in [0.006, 0.041]$ to investigate the response of attractive colloidal dispersions to mechanical shear. These experiments involved rapidly changing the shear rate from high to low values, revealing a microstructural scenario depicted in Fig. 5.

In the hydrodynamic regime, attractive CB particles assemble into clusters with a fractal dimension of $d_f = 2.35$, and their size inversely scales with the shear rate as $\xi_c \propto \dot{\gamma}^{-m}$, where m is approximately equal to 0.5. The size of these clusters is primarily determined by the fluid stress, represented by $\sigma = \eta_f \dot{\gamma}$, where η_f is the fluid background viscosity. The viscous contribution of the clusters can be approximated by the one of a hard sphere dispersion and the viscosity of CB dispersions can be calculated using the Krieger-Dougherty equation, provided we replace the CB particle volume fraction ϕ_{r0} by an effective volume fraction of clusters ϕ_{eff} . This hydrodynamic regime persists down to a critical point characterized by coordinates $(\dot{\gamma}^*, \sigma^*)$. Although this model captures well the interplay between structure and rheology, the dynamics underlying this process remain to be fully understood. Specifically, what mechanisms drive cluster growth as the shear rate decreases? It might involve a balance between the aggregation of clusters upon collision and a feedback erosion process driven by the shear rate that restricts cluster size⁷³.

At this juncture point $(\dot{\gamma}^*, \sigma^*)$, the cluster growth stops and their effective volume fraction stabilizes at $\phi_{\text{eff}} \approx 0.39$, irrespective of ϕ_{r0} . We propose that at ϕ_{eff}^* , clusters percolate into a dynamic network. This hypothesis gains support from the observation that σ^* closely tracks variations in the dynamical yield stress σ_y . When ϕ_{r0} increases, the clusters size at percolation decreases, leading to a higher σ_y . In essence, the properties of dispersions in the limit where $\dot{\gamma} = 0$ are inherited from the percolation point. As a result, the dynamic percolation point is a key parameter to explain the mechanical response of CB dispersions under shear. While the cluster growth in the hydrodynamic regime proceeds independently of the volume fraction, the percolation of clusters at a constant ϕ_{eff}^* determines both the critical shear rate and the yield stress of the flow curve.

Microstructural models have traditionally partitioned the stress response of attractive dispersions into an hydrodynamic and an elastic contributions^{29,30} and a robust and self-consistent comprehension of these two regimes has been established for CB dispersions. However, in Fig. 4a, it is clear that the hydrodynamic regime does not extend to low shear rates, in the vicinity of σ_y , and that an additional contribution is required to model the flow curve at intermediate shear rates ($\dot{\gamma} < \dot{\gamma}^*$). Previously, we have stressed that the cluster size at percolation was maintained when $\dot{\gamma}$ is further decreased. It pictures the idea that, during the intermediate regime, the structure of the dispersion is shear-independent and composed of large and crowded clusters, comparable with the flow of adhesive non-Brownian dispersions. Based on the phenomenological model of Wyart and Cates⁷⁴, constraint-based rheology was shown to successfully model all types of

flow curves⁷⁵. In this framework, particle sliding and rolling are constrained by adhesive and/or frictional contacts that are accounted by a shear-dependent jamming point ϕ_m . For adhesive non-Brownian dispersions, experimental results⁷⁶ highlight the coupling between adhesion and friction to account for the shear-thinning and yield stress of the dispersions. In the case of attractive Brownian dispersions, for $\dot{\gamma} < \dot{\gamma}^*$, the flow of sticky clusters may be successfully modeled using constraint-based rheology. The challenge probably lies in rationalizing the contribution of adhesion and friction in these systems. An alternative method for modeling this plastic regime would involve describing the elastic stress contribution of the dynamic network with a network percolation loss rate that decreases with respect to a characteristic time of $1/\dot{\gamma}$.

Additional research is needed to characterize the intermediate regime. Colloidal systems that are optically transparent would be particularly advantageous, as they would allow for the characterization of mesoscopic structures (with $\xi > 2 \mu\text{m}$) using optical microscopy or dynamic light scattering. Besides, measuring the viscoelastic properties of the suspensions during shear using orthogonal superposition rheometry⁷⁷ may bring further insights to the shear stress contribution during flow curve tests. Finally, it would be beneficial to validate the approach used in this paper and compare our findings with those from other attractive colloidal systems subjected to flow. Given the thixotropic behavior of Carbon black dispersions and attractive colloidal dispersions in general, it would also be interesting to study the impact of the flow curve protocol in such frameworks. We have indeed opted to continuously decrease the shear rate. If we were to continuously decrease the shear stress instead, would the control parameter still be the shear rate? Alternatively, one could perform discrete jumps from a higher shear rate to a lower one. In this scenario, would the cluster size be determined by the initial or final value of the shear rate? It is observed that at lower shear rates, the viscosity decreases over time⁷⁷. Is this behavior attributed to slip at the boundaries of the Couette cell or to the restructuring of the clusters and the network over time?

AUTHOR CONTRIBUTIONS

JB and TG carried out the experiments. JB analysed the data. TG, LVB and AP helped JB analyzing the data. TG and JB wrote the paper. TG designed and managed the project.

CONFLICTS OF INTEREST

There are no conflicts to declare.

ACKNOWLEDGEMENTS

The authors are especially grateful to the ESRF for beamtime at the beamline ID02 (proposal SC-5236) and Theyencheri Narayanan for the discussions and technical support during the USAXS measurements. The authors thank

Szilvia Karpati (ENS de Lyon) and the CIQLE (Centre d'Imagerie Quantitative Lyon-Est) microscopy platform for their help with the electron microscopy imaging of the CB particles. The authors express their appreciation for valuable discussions held with Thibaut Divoux and Sébastien Manneville. This work was supported by the Région Auvergne-Rhône-Alpes "Pack Ambition Recherche", the LABEX iMUST (ANR-10-LABX-0064) of Université de Lyon, within the program "Investissements d'Avenir" (ANR-11-IDEX-0007), the ANR grants (ANR-18-CE06-0013 and ANR-21-CE06-0020-01). This work benefited from meetings within the French working group GDR CNRS 2019 "Solliciter LA Matière Molle" (SLAMM).

V. APPENDIX

A. Effect of the duration on the flow curve

As shown in Fig. 6, the shape of the flow curve depends on the shear duration Δt applied to measure each point. Two regimes can be distinguished depending on the shear rate: at high shear rate ($\dot{\gamma} > 1 \text{ s}^{-1}$), the stress response is independent on Δt while at low shear rate ($\dot{\gamma} < 1 \text{ s}^{-1}$) and for high volume fractions of CB particles ϕ_{r0} , a drop of the stress can be observed. The drop is all the more important that Δt is large.

B. Herschel-Bulkley model

In Fig. 7, the Herschel-Bulkley model provides an acceptable fit of the data. However the Herschel-Bulkley model is less efficient than the CTS model to capture the data at intermediate shear rate, around $\dot{\gamma} \approx 1 \text{ s}^{-1}$. Notably, the critical shear rate $\dot{\gamma}_{HB}^*$ shows a different scaling with ϕ_{r0} in com-

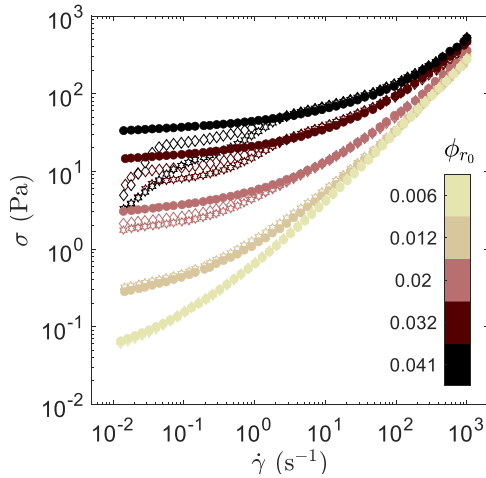


FIG. 6. Flow curve of carbon black dispersions at various volume fraction ϕ_{r0} . The ramp was conducted with $\Delta t = 1$ (circle), 50 (diamond) and 100 (star) s/pts.

parison with $\dot{\gamma}^*$ obtained from the CTS model (Fig. 7c). As pointed in⁵⁸, the CTS model gets rid of the nonphysical power exponent n (Fig. 7d) by introducing a high shear viscosity η_0 (Eq. 7).

C. Form factor

The form factor of the CB particles was measured with SAXS on a diluted sample ($\phi_{r0} = 10^{-4}$) at rest and fitted using different models.

In Fig. 8a, the form factor of the CB particles is described as a combination of a particle form factor $P(q)$, accounting for the nodules, and a fractal structure factor $S(q)$, accounting for the primary aggregates, with $I(q) \propto P(q)S(q)$. $P(q)$ is modeled as the form factor of polydisperse spheres with a log-normal distribution⁷⁸ and $S(q)$ is modeled as a mass fractal structure factor⁷⁹. The fit yields $a = 3 \text{ nm}$, $r_0 = 33 \text{ nm}$, $d_{fr0} = 2.85$. The radius of gyration of a fractal aggregate is given by⁷⁹: $r_0^2 = \frac{d_f(d_f+1)\xi_0^2}{2}$ which yields $r_0 = 76 \text{ nm}$.

In Fig. 8b, the form factor of the CB particles is modeled using a two-level Beaucage model. The first level models the particles of size $a = 20 \text{ nm}$. The second level models the primary aggregate of size $\xi_{r0} = 85 \text{ nm}$ and fractal dimension $d_{fr0} = 2.78$.

In both cases, the fit results compares well with the CB particles TEM images in Fig. 8c. The characterization of the Vulcan PF particles presented here confirms that these particles are small and compact in comparison with other CB particles previously reported (e.g. $R_g \approx 180 \text{ nm}$ for Vulcan XC-72^{48,52}).

D. Anisotropy

Fig. 9 displays the scattering curves of CB dispersions, azimuthally averaged either in the flow direction or in the vorticity direction. For the blue-green curves, corresponding to the vorticity direction, the low q region is reduced because of the rectangular shape of the beamstop used. At all shear rates, the superimposition of the curves in both directions indicates the absence of anisotropic structure, also reported by¹⁹ for CB dispersions in oil.

E. Modified Beaucage model

The intensity spectrum $I(q)$ may be fitted by a modified two-level Beaucage model^{49,50,67,80,81} through:

$$I(q) = I_c(q)S_S(q) + I_{r0}(q) \quad (9)$$

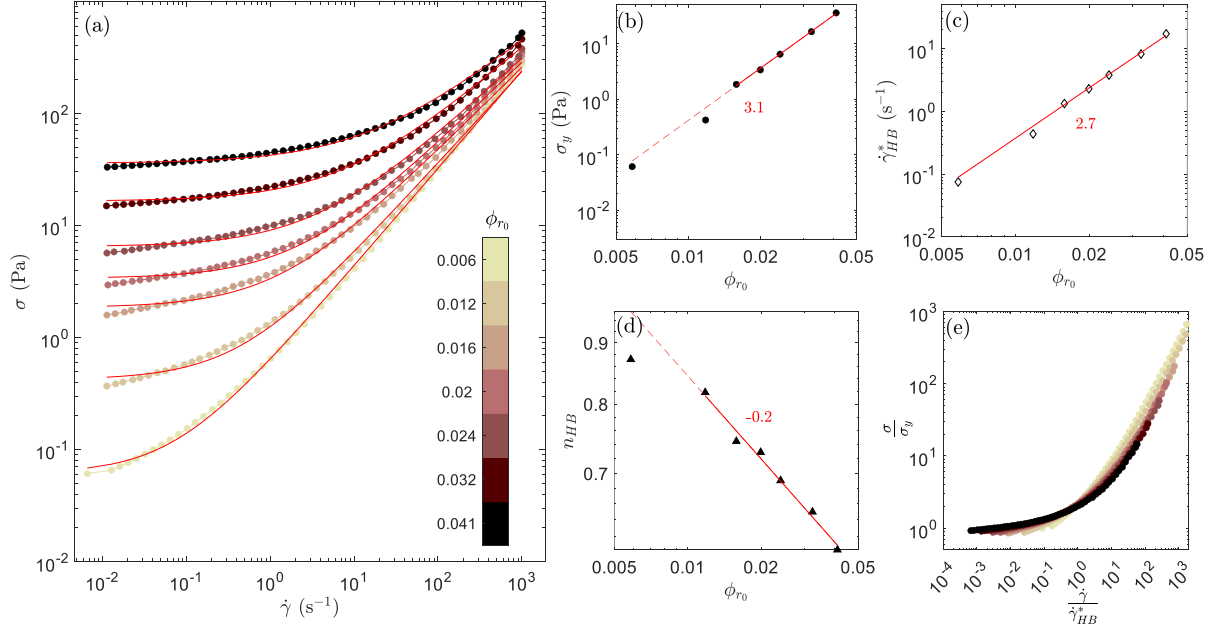


FIG. 7. Herschel-Bulkley model of the carbon black flow curves. (a) Shear stress σ vs shear rate $\dot{\gamma}$ during fast flow curves of carbon black dispersions at various volume fraction of CB particles ϕ_{r0} . Inset displays the dynamic viscosity η vs $\dot{\gamma}$. The red curves correspond to the best fits with the Herschel-Bulkley component model (eq. 4). (b)-(d) Evolution of the parameters of the Herschel-Bulkley model with ϕ_{r0} . σ_y is the apparent yield stress, $\dot{\gamma}_{HB}^*$ is a critical shear rate and n is the power exponent. Red lines are the best power law fit of the data. (e) Normalized flow curves: σ/σ_y vs $\dot{\gamma}/\dot{\gamma}_{HB}^*$.

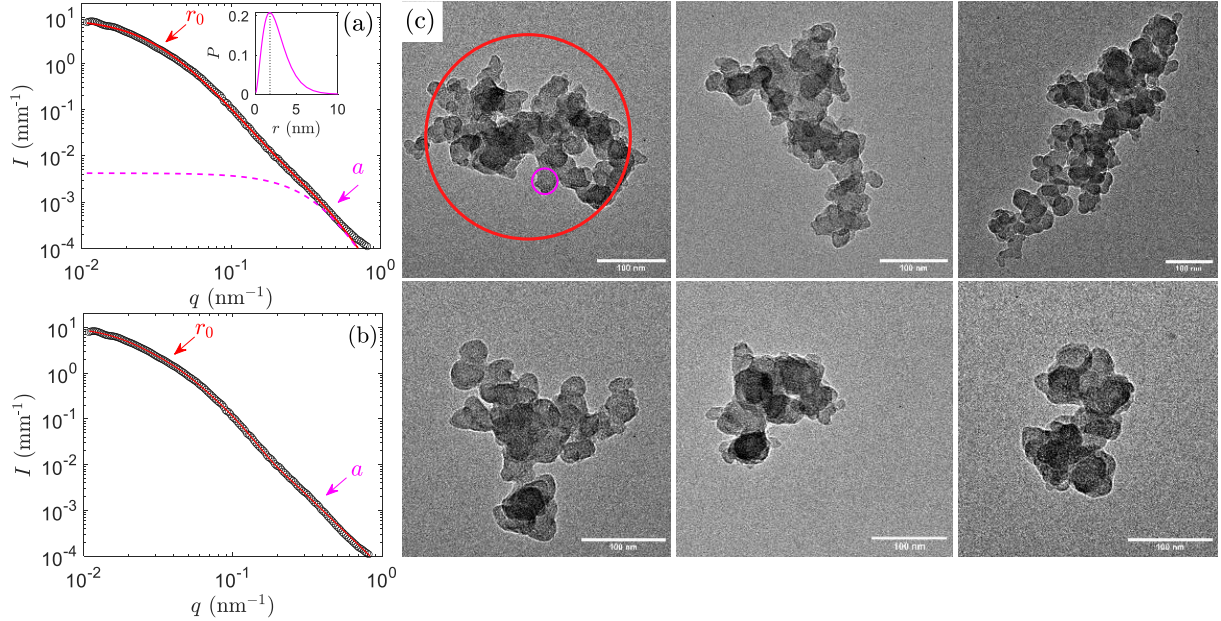


FIG. 8. Characterization of the Vulcan[®]PF carbon black (CB) particles. (a) Fit of the CB form factor using a mass fractal model. Inset: log-normal distribution of a . (b) Fit of the CB form factor using a Beaucage model. Form factor of the CB particles measured by SAXS for $\phi_{r0} = 10^{-4}$. CB particles are composed of nodules of radius a that are fused to form primary aggregates of radius r_0 . (c) Representative set of TEM images of individual CB particles.

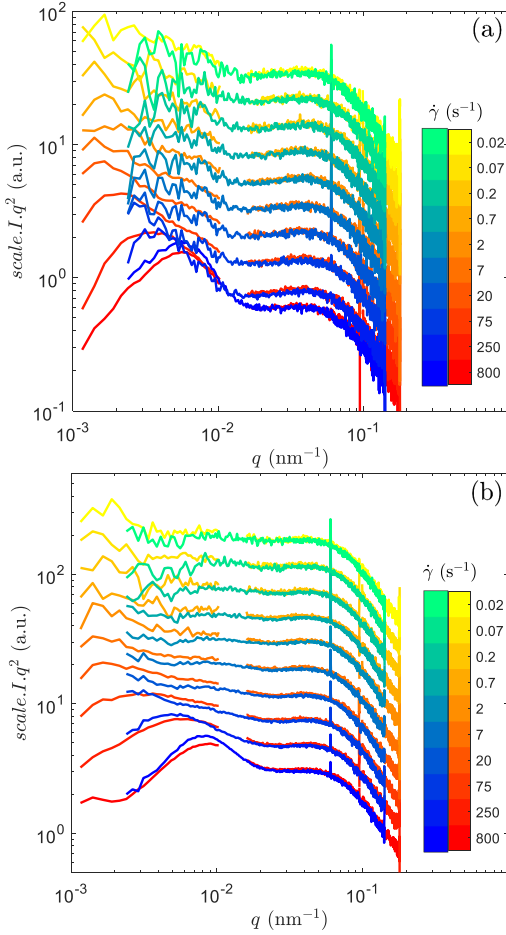


FIG. 9. Comparison of the scattering intensity between the flow direction (red-yellow) and the vorticity direction (blue-green) at $\phi_{r0} = 0.006$ (a) and 0.032 (b). The color gradients code for the shear rate.

with

$$\begin{cases} I_c(q) = G_c e^{\left(-\frac{q^2 \xi_c^2}{3}\right)} + B_c e^{\left(-\frac{q^2 r_0^2}{3}\right)} \text{erf}\left(\frac{q \xi_c}{\sqrt{6}}\right)^{-3d_f} q^{-d_f} \\ S_s(q) = 1 + C_s \left(\left(\frac{q \xi_s}{2\pi} \right)^2 + \left(\frac{2\pi}{q \xi_s} \right)^2 \right)^{-1} \\ I_{r0}(q) = G_{r0} e^{\left(-\frac{q^2 r_0^2}{3}\right)} + B_{r0} \text{erf}\left(\frac{q r_0}{\sqrt{6}}\right)^{-3d_{r0}} q^{-d_{r0}} \end{cases} \quad (10)$$

This model accounts for the presence of three distinct bumps observed in $I(q)$ corresponding to the length scales r_0 , ξ_s , and ξ_c arranged in ascending order. The two-level Beaucage model combines the scattering contribution $I_c(q)$ from the clusters with a size ξ_c and a fractal dimension d_f with the contribution $I_{r0}(q)$ from the CB particle of size r_0 . To account for the intermediate length scale ξ_s , revealed at low shear rate, the cluster intensity $I_c(q)$ is multiplied by an ad-hoc structure factor $S_s(q)$, resulting in an increase in scattering at intermediate q . This structure factor $S_s(q)$ is a function that exhibits a peak at $q_s = 2\pi/\xi_s$ and reaches a maximum value of $1 + C_s/2$. Away from $q_s = 2\pi/\xi_s$, it gradually converges

to 1. While this choice of $S_s(q)$ is straightforward, it is not entirely satisfactory as it fails to meet thermodynamic limits. Specifically, $S_s(q \rightarrow 0)$ equals 1, whereas it should be proportional to the isothermal compressibility. In Fig. 10, we show the fit of the scattering intensity of the CB dispersions using the modified two-level Beaucage model.

Hipp et al.¹⁹ also study the formation of sheared clusters of carbon black particles. They have characterized the cluster properties using small angle neutron scattering (SANS) and fit their data with the following model:

$$I(q) = P(q) S_1(q) S_2(q) \quad (11)$$

with

$$\begin{cases} P(q) = \begin{cases} \frac{G}{q^s} \exp\left(\frac{-q^2 R_g^2}{3-s}\right) & q \leq q_1, \\ \frac{D}{q^m} & q \geq q_1 \end{cases} \\ S_i(q) = 1 + \frac{d_f \Gamma(d_f - 1)}{[1 + 1/(q \xi)^2]^{(d_f - 1)/2}} \frac{\sin[(d_f - 1) \tan^{-1}(q \xi)]}{(q R_0)^{d_f}} \end{cases} \quad (12)$$

where $P(q)$ is the form factor of the nodule (Guinier Porod) of size a . $S_1(q)$ is a mass fractal model⁷⁹ used to fit the form factor of the CB particles as inseparable fractal cluster of size r_0 and fractal dimension d_{fr0} composed of spheres of size a . $S_2(q)$ is a mass fractal model⁷⁹ used to fit fractal clusters of size ξ_c and fractal dimension d_f composed of the CB particles. Although the CB particles and the solvent used by Hipp et al. differ from ours, we attempted to fit our data with their model. In contrast to the modified two-level Beaucage model, the Hipp et al. model does not incorporate the intermediate length scale ξ_s . As depicted in Fig. 11, the Hipp et al. model does not provide a good fit to the SAXS data, it misses by construction ξ_s and tends to underestimate ξ_c . This justifies our preference for the modified Beaucage model over the model proposed by Hipp et al.¹⁹

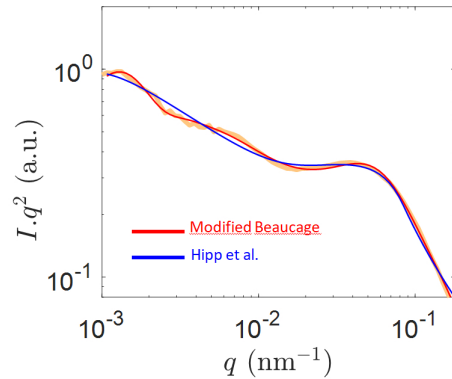


FIG. 11. Comparison between the modified Beaucage model and the Hipp et al. model.

F. Evolution of ξ_c with σ

In Fig. 12, we observe that ξ_c does not scale with σ .

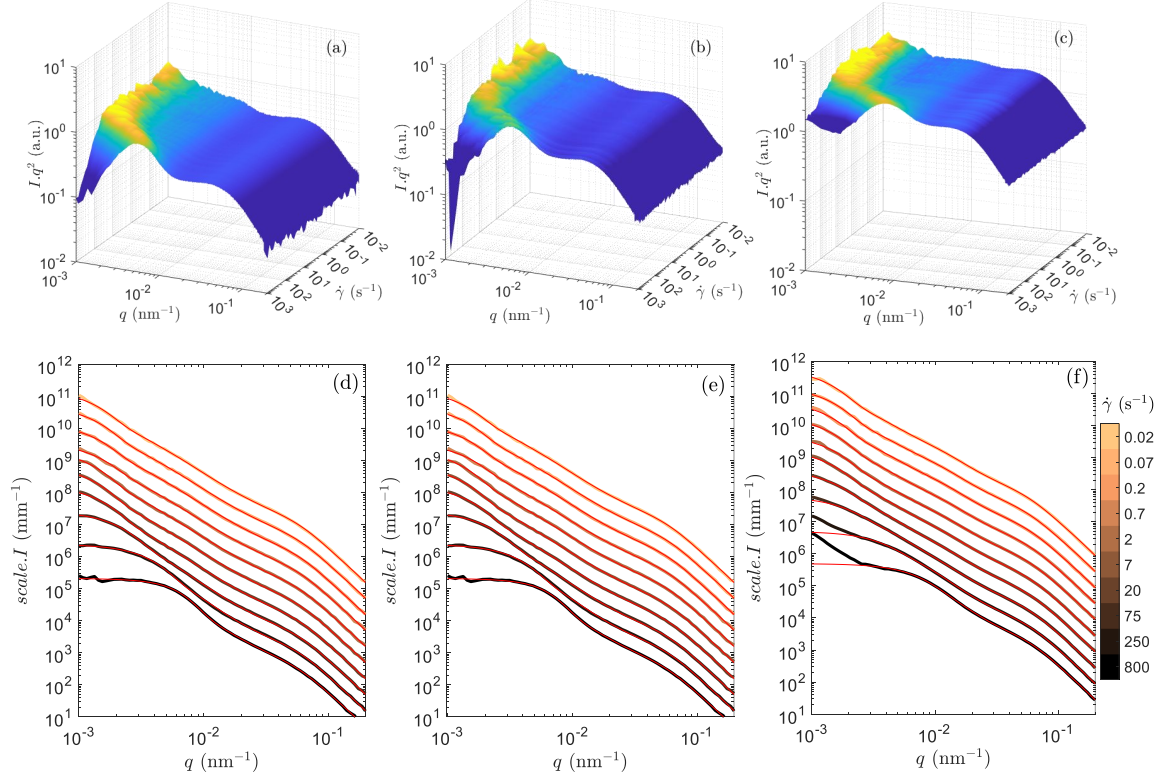


FIG. 10. (a)-(c) 3D visualization of the shear dependence of the scattering intensity in Kratky representation Iq^2 vs q for the volume fractions $\phi_{r0} = 0.006$ (a), 0.012 (b) and 0.032 (c). The color gradient codes for the intensity of Iq^2 . (d)-(f) $I(q)$ and their fit (red lines) using the modified Beaucage model (Eq. 10) for the volume fractions $\phi_{r0} = 0.006$ (d), 0.012 (e) and 0.032 (f). The color gradient from light orange to black codes for the shear rate. $I(q)$ are shifted along the y -axis for better visualization.

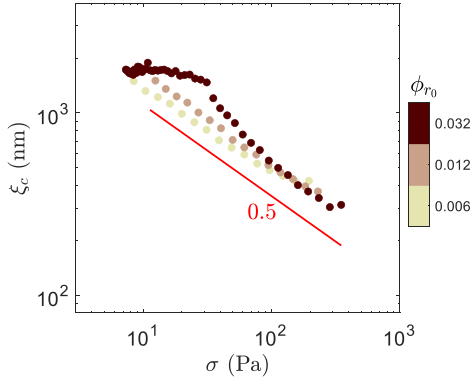


FIG. 12. Evolution of ξ_c with σ for $\phi_{r0} = 0.006, 0.012$ and 0.032 . Red line is a power law $\xi \propto \sigma^{-0.5}$ displayed for comparison.

G. Structure factor

The structure factor of the CB dispersion $S(q, \phi_{r0}) = \frac{I(q, \phi_{r0})}{P(q)} \frac{\phi_{r0}^P}{\phi_{r0}}$ is obtained by dividing the the scattering intensity of the CB dispersion at ϕ_{r0} by the CB particles form factor measured at $\phi_{r0}^P = 10^{-4}$ as shown in Fig 8. $S(q)$ displays an anticorrelation peak at $q \sim 0.03 \text{ nm}^{-1}$, associated with attractive interactions among the CB particles the background oil.

H. Evolution of ξ_s and ξ_c with ϕ_{r0} and $\dot{\gamma}$

The dependence of the length scales ξ_s and ξ_c with ϕ_{r0} and $\dot{\gamma}$ was investigated using (i) a model free analysis (Eq. 8) and (ii) a two-level modified Beaucage model (Eq. 10). ξ_s and ξ_c are displayed as function of $\dot{\gamma}$ on Fig. 14b-c. Both approaches show that for $\dot{\gamma} > 50 \text{ s}^{-1}$, ξ_c increases with $\dot{\gamma}$ as $\xi_c \propto \dot{\gamma}^{-m}$ with $m \approx 0.5$, highlighting the robustness of this result. Below $\dot{\gamma} = 50 \text{ s}^{-1}$, ξ_c is found to be constant ($1 < \xi_c < 2 \text{ }\mu\text{m}$) at $\phi_{r0} = 0.032$. For lower volume fraction we believe the cluster size increases beyond the range of length scales that can be probed by the SAXS set-up. In the microstructural analysis

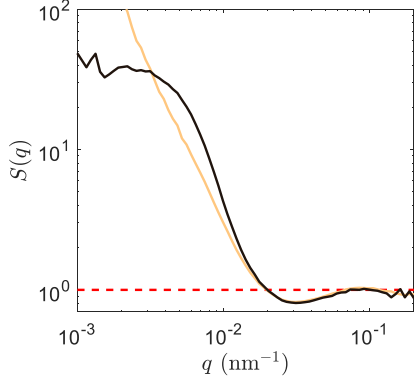


FIG. 13. Comparison of the structure factor $S(q)$ of the CB dispersion at $\phi_{r0} = 0.006$ at $\dot{\gamma} = 800$ (black) and 0.02 s^{-1} (light orange).

developed in section III for the Fig. 4, we have extrapolated the values of ξ_c using $\xi_c \propto \dot{\gamma}^{-m}$ up to the limit when $\sigma_h > \sigma$.

In Fig. 14b-c, ξ_s is found to be independent of the shear rate and slightly diminishes as ϕ_{r0} increases. The dependence of ξ_s with ϕ_{r0} is also illustrated in Fig. 14a.

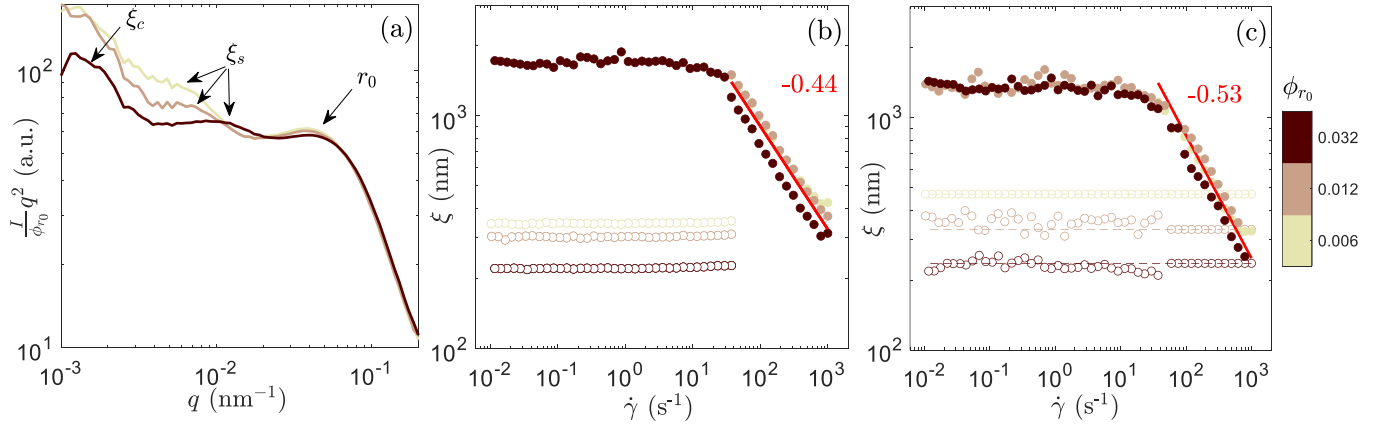


FIG. 14. (a) Rescaled scattering curve $I(q)/\phi r_0$ vs q measured under low shear rate at $\dot{\gamma} = 0.02 \text{ s}^{-1}$ for $\phi r_0 = 0.006, 0.012$ and 0.032 . (b)-(c) Cluster size ξ_c (solid circles) and intermediary length ξ_s (empty circles) as function of the shear $\dot{\gamma}$ determined from the model-free analysis (b) and the modified two-level Beaucage model (c). Red lines are the best power law fit of ξ_c vs $\dot{\gamma}$ for $\dot{\gamma} > 50 \text{ s}^{-1}$.

- ¹A. Chougnnet, T. Palermo, A. Audibert, and M. Moan, "Rheological behaviour of cement and silica suspensions: Particle aggregation modelling," *Cement and Concrete Research* **38**, 1297–1301 (2008).
- ²S. Morariu, M. Teodorescu, and M. Bercea, "Rheological investigation of polymer/clay dispersions as potential drilling fluids," *Journal of Petroleum Science and Engineering* **210**, 110015 (2022).
- ³M. S. Alfonso, H. Parant, J. Yuan, W. Neri, E. Laurichesse, K. Kampioti, A. Colin, and P. Poulin, "Highly conductive colloidal carbon based suspension for flow-assisted electrochemical systems," *iScience* **24**, 102456 (2021).
- ⁴D. B. Genovese, J. E. Lozano, and M. A. Rao, "The rheology of colloidal and noncolloidal food dispersions," *Journal of Food Science* **72** (2007), 10.1111/j.1750-3841.2006.00253.x.
- ⁵Z. Xi, W. Liu, D. J. McClements, and L. Zou, "Rheological, structural, and microstructural properties of ethanol induced cold-set whey protein emulsion gels: Effect of oil content," *Food Chemistry* **291**, 22–29 (2019).
- ⁶J. Mewis and N. J. Wagner, "Colloidal suspension rheology," *Colloidal Suspension Rheology* **978052151515**, 1–393 (2011).
- ⁷S. Lazzari, L. Nicoud, B. Jaquet, M. Lattuada, and M. Morbidelli, "Fractal-like structures in colloid science," *Advances in Colloid and Interface Science* **235**, 1–13 (2016).
- ⁸A. Zaccone, H. Winter, M. Siebenbürger, and M. Ballauff, "Linking self-assembly, rheology, and gel transition in attractive colloids," *Journal of Rheology* **58**, 1219–1244 (2014).
- ⁹M. Haw, M. Sievwright, W. C. Poon, and P. Pusey, "Cluster-cluster gelation with finite bond energy," *Advances in colloid and interface science* **62**, 1–16 (1995).
- ¹⁰D. Xie, H. Wu, A. Zaccone, L. Braun, H. Chen, and M. Morbidelli, "Criticality for shear-induced gelation of charge-stabilized colloids," *Soft Matter* **6**, 2692–2698 (2010).
- ¹¹D. Weitz and M. Oliveria, "Fractal structures formed by kinetic aggregation of aqueous gold colloids," *Physical review letters* **52**, 1433 (1984).
- ¹²D. W. Schaefer, J. E. Martin, P. Wiltzius, and D. S. Cannell, "Fractal geometry of colloidal aggregates," *Physical Review Letters* **52**, 2371 (1984).
- ¹³V. Trappe and P. Sandkühler, "Colloidal gels—low-density disordered solid-like states," *Current opinion in colloid & interface science* **8**, 494–500 (2004).
- ¹⁴R. C. Sonntag and W. B. Russel, "Structure and breakup of flocs subjected to fluid stresses. I. Shear experiments," *Journal of Colloid And Interface Science* **113**, 399–413 (1986).
- ¹⁵A. Zaccone, M. Soos, M. Lattuada, H. Wu, M. U. Bäbler, and M. Morbidelli, "Breakup of dense colloidal aggregates under hydrodynamic stresses," *Physical Review E - Statistical, Nonlinear, and Soft Matter Physics* **79**, 061401 (2009).
- ¹⁶R. Massaro, G. Colombo, P. Van Puyvelde, and J. Vermant, "Viscoelastic cluster densification in sheared colloidal gels," *Soft Matter* **16**, 2437–2447 (2020).
- ¹⁷J. Mewis and N. J. Wagner, "Thixotropy," *Advances in Colloid and Interface Science* **147-148**, 214–227 (2009).
- ¹⁸Z. Varga and J. W. Swan, "Large scale anisotropies in sheared colloidal gels," *Journal of Rheology* **62**, 405–418 (2018).
- ¹⁹J. B. Hipp, J. J. Richards, and N. J. Wagner, "Direct measurements of the microstructural origin of shear-thinning in carbon black suspensions," *Journal of Rheology* **65**, 145–157 (2021).
- ²⁰L.-V. Bouthier, R. Castellani, S. Manneville, A. Poulesquen, R. Valette, and E. Hachem, "Aggregation and disaggregation processes in clusters of particles under flow: Simple numerical and theoretical insights," *Physical Review Fluids* **8**, 023304 (2023).
- ²¹R. Wessel and R. C. Ball, "Fractal aggregates and gels in shear flow," *Physical Review A* **46**, 3008–3011 (1992).
- ²²P. Snabre and P. Mills, "I. Rheology of weakly flocculated suspensions of rigid particles," *Journal de Physique III* **6**, 1811–1834 (1996).
- ²³A. A. Potanin, "On the computer simulation of the deformation and breakup of colloidal aggregates in shear flow," *Journal of colloid and interface science* **157**, 399–410 (1993).
- ²⁴R. J. Hunter and J. Frayne, "Flow behavior of coagulated colloidal sols. v. dynamics of floc growth under shear," *Journal of Colloid and Interface Science* **76**, 107–115 (1980).
- ²⁵L. Brakalov, "A connection between the orthokinetic coagulation capture efficiency of aggregates and their maximum size," *Chemical Engineering Science* **42**, 2373–2383 (1987).
- ²⁶X. Ruan, S. Chen, and S. Li, "Structural evolution and breakage of dense agglomerates in shear flow and Taylor-Green vortex," *Chemical Engineering Science* **211**, 115261 (2020).
- ²⁷W. H. Herschel and R. Bulkley, "Konsistenzmessungen von gummi-benzollösungen," *Kolloid-Zeitschrift* **39**, 291–300 (1926).
- ²⁸R. I. Jeldres, P. D. Fawell, and B. J. Florio, "Population balance modelling to describe the particle aggregation process: A review," *Powder technology* **326**, 190–207 (2018).
- ²⁹R. De Rooij, A. A. Potanin, D. Van Den Ende, and J. Mellema, "Transient shear viscosity of weakly aggregating polystyrene latex dispersions," *The Journal of Chemical Physics* **100**, 5353–5360 (1994).
- ³⁰A. A. Potanin, R. De Rooij, D. Van Den Ende, and J. Mellema, "Micro-rheological modeling of weakly aggregated dispersions," *The Journal of Chemical Physics* **102**, 5845–5853 (1995).
- ³¹W. Wolthers, M. H. G. Duits, D. van den Ende, and J. Mellema, "Shear history dependence of the viscosity of aggregated colloidal dispersions," *Journal of Rheology* **40**, 799–811 (1996).
- ³²D. Quemada and C. Berli, "Energy of interaction in colloids and its implications in rheological modeling," *Advances in colloid and interface science* **98**, 51–85 (2002).
- ³³L. Silbert, J. Melrose, and R. Ball, "The rheology and microstructure of concentrated, aggregated colloids," *Journal of Rheology* **43**, 673–700 (1999).
- ³⁴P. Varadan and M. J. Solomon, "Shear-induced microstructural evolution of a thermoreversible colloidal gel," *Langmuir* **17**, 2918–2929 (2001).
- ³⁵D. Quemada, "Rheology of concentrated disperse systems II. A model for non-newtonian shear viscosity in steady flows," *Rheologica Acta* **17**, 632–642 (1978).
- ³⁶D. B. Genovese, "Shear rheology of hard-sphere, dispersed, and aggregated suspensions, and filler-matrix composites," *Advances in Colloid and Interface Science* **171-172**, 1–16 (2012).
- ³⁷I. M. Krieger and T. J. Dougherty, "A Mechanism for Non-Newtonian Flow in Suspensions of Rigid Spheres," *Transactions of the Society of Rheology* **3**, 137–152 (1959).
- ³⁸T. Gibaud, T. Divoux, and S. Manneville, "Encyclopedia of Complexity and Systems Science," (Springer, 2020) Chap. Nonlinear mechanics of colloidal gels: creep, fatigue and shear-induced yielding, pp. 1–24.
- ³⁹J. J. Richards, P. Z. Ramos, and Q. Liu, "A review of the shear rheology of carbon black suspensions," *Frontiers in Physics*, 1–11 (2023).
- ⁴⁰V. Trappe and D. A. Weitz, "Scaling of the viscoelasticity of weakly attractive particles," *Physical Review Letters* **85**, 449–452 (2000).
- ⁴¹G. Ovarlez, L. Tocquer, F. Bertrand, and P. Coussot, "Rheopexy and tunable yield stress of carbon black suspensions," *Soft Matter* **9**, 5540–5549 (2013).
- ⁴²A. Helal, T. Divoux, and G. H. McKinley, "Simultaneous rheoelectric measurements of strongly conductive complex fluids," *Physical Review Applied* **6**, 064004 (2016).
- ⁴³J. B. Hipp, J. J. Richards, and N. J. Wagner, "Structure-property relationships of sheared carbon black suspensions determined by simultaneous rheological and neutron scattering measurements," *Journal of Rheology* **63**, 423–436 (2019).
- ⁴⁴T. Gibaud, D. Frelat, and S. Manneville, "Heterogeneous yielding dynamics in a colloidal gel," *Soft Matter* **6**, 3482–3488 (2010).
- ⁴⁵V. Grenard, T. Divoux, N. Taberlet, and S. Manneville, "Timescales in creep and yielding of attractive gels," *Soft matter* **10**, 1555–1571 (2014).
- ⁴⁶T. Gibaud, C. Perge, S. B. Lindström, N. Taberlet, and S. Manneville, "Multiple yielding processes in a colloidal gel under large amplitude oscillatory stress," *Soft Matter* **12**, 1701–1712 (2016).
- ⁴⁷C. Perge, N. Taberlet, T. Gibaud, and S. Manneville, "Time dependence in large amplitude oscillatory shear: A rheo-ultrasonic study of fatigue dynamics in a colloidal gel," *Journal of Rheology* **58**, 1331–1357 (2014).
- ⁴⁸J. J. Richards, J. B. Hipp, J. K. Riley, N. J. Wagner, and P. D. Butler, "Clustering and Percolation in Suspensions of Carbon Black," *Langmuir* **33**, 12260–12266 (2017).
- ⁴⁹N. Dages, L. V. Bouthier, L. Matthews, S. Manneville, T. Divoux, A. Poulesquen, and T. Gibaud, "Interpenetration of fractal clusters drives elasticity in colloidal gels formed upon flow cessation," *Soft Matter* **18**, 6645–6659 (2022), arXiv:2203.08675.
- ⁵⁰L.-V. Bouthier and T. Gibaud, "Three length-scales colloidal gels: The clus-

- ters of clusters versus the interpenetrating clusters approach,” *Journal of Rheology* **67**, 621–633 (2023).
- ⁵¹T. Gibaud, N. Dagès, P. Lidon, G. Jung, L. C. Ahouré, M. Sztucki, A. Poulesquen, N. Hengl, F. Pignon, and S. Manneville, “Rheoacoustic Gels: Tuning Mechanical and Flow Properties of Colloidal Gels with Ultrasonic Vibrations,” *Physical Review X* **10**, 1–21 (2020), 011028, 1905.07282.
 - ⁵²N. Dagès, P. Lidon, G. Jung, F. Pignon, S. Manneville, and T. Gibaud, “Mechanics and structure of carbon black gels under high-power ultrasound,” *Journal of Rheology* **65**, 477–490 (2021), arXiv:2011.06809.
 - ⁵³L. Liu, Z. Shen, X. Zhang, and H. Ma, “Highly conductive graphene/carbon black screen printing inks for flexible electronics,” *Journal of colloid and interface science* **582**, 12–21 (2021).
 - ⁵⁴H. Li, H.-g. Xiao, and J.-p. Ou, “Effect of compressive strain on electrical resistivity of carbon black-filled cement-based composites,” *Cement and Concrete Composites* **28**, 824–828 (2006).
 - ⁵⁵Q. Liu and J. J. Richards, “Rheo-electric measurements of carbon black suspensions containing polyvinylidene difluoride in n-methyl-2-pyrrolidone,” *Journal of Rheology* **67**, 647–659 (2023).
 - ⁵⁶P. Panine, M. Gradzielski, and T. Narayanan, “Combined rheometry and small-angle x-ray scattering,” *Review of Scientific Instruments* **74**, 2451–2455 (2003).
 - ⁵⁷T. Divoux, V. Grenard, and S. Manneville, “Rheological hysteresis in soft glassy materials,” *Physical Review Letters* **110**, 1–7 (2013), arXiv:1207.3953.
 - ⁵⁸M. Caggioni, V. Trappe, and P. T. Spicer, “Variations of the Herschel–Bulkley exponent reflecting contributions of the viscous continuous phase to the shear rate-dependent stress of soft glassy materials,” *Journal of Rheology* **64**, 413–422 (2020).
 - ⁵⁹T. Narayanan, M. Sztucki, T. Zinn, J. Kieffer, A. Homs-Puron, J. Gorini, P. Van Vaerenbergh, and P. Boesecke, “Performance of the time-resolved ultra-small-angle x-ray scattering beamline with the extremely brilliant source,” *Journal of Applied Crystallography* **55**, 98–111 (2022).
 - ⁶⁰E. M. Dannenberg, L. Paquin, and H. Gwinnell, “Carbon Black,” in *Kirk-Othmer Encyclopedia of Chemical Technology* (John Wiley & Sons, Ltd, 2000).
 - ⁶¹A. Einstein, *Eine neue bestimmung der moleküldimensionen*, Ph.D. thesis, ETH Zurich (1905).
 - ⁶²J.-M. Piau, M. Dorget, J.-F. Palierne, and A. Pouchelon, “Shear elasticity and yield stress of silica–silicone physical gels: Fractal approach,” *Journal of Rheology* **43**, 305–314 (1999).
 - ⁶³G. P. Baeza, A. C. Genix, C. Degrandcourt, L. Petitjean, J. Gummel, M. Couty, and J. Oberdisse, “Multiscale filler structure in simplified industrial nanocomposite silica/SBR systems studied by SAXS and TEM,” *Macromolecules* **46**, 317–329 (2013).
 - ⁶⁴L.-V. Bouthier and T. Gibaud, “Three length scales colloidal gels: the clusters of clusters versus the interpenetrating clusters approach,” arXiv (2022), arXiv:2210.10505.
 - ⁶⁵M. Carpineti, M. Giglio, and V. Degiorgio, “Mass conservation and anti-correlation effects in the colloidal aggregation of dense solutions,” *Physical Review E* **51**, 590 (1995).
 - ⁶⁶T. Narayanan, R. Dattani, J. Möller, and P. Kwaśniewski, “A microvolume shear cell for combined rheology and x-ray scattering experiments,” *Review of Scientific Instruments* **91** (2020).
 - ⁶⁷B. Keshavarz, D. G. Rodrigues, J. B. Champenois, M. G. Frith, J. Ilavsky, M. Geri, T. Divoux, G. H. McKinley, and A. Poulesquen, “Time-connectivity superposition and the gel/glass duality of weak colloidal gels,” *Proceedings of the National Academy of Sciences of the United States of America* **118** (2021), 10.1073/pnas.2022339118.
 - ⁶⁸B. O. Conchuir, Y. M. Harshe, M. Lattuada, and A. Zaccone, “Analytical model of fractal aggregate stability and restructuring in shear flows,” *Industrial and Engineering Chemistry Research* **53**, 9109–9119 (2014).
 - ⁶⁹L. Ehrl, M. Soos, and M. Lattuada, “Generation and geometrical analysis of dense clusters with variable fractal dimension,” *Journal of Physical Chemistry B* **113**, 10587–10599 (2009).
 - ⁷⁰J. A. Richards, R. E. O’Neill, and W. C. Poon, “Turning a yield-stress calcite suspension into a shear-thickening one by tuning inter-particle friction,” *Rheologica Acta* **60**, 97–106 (2021), arXiv:2007.05433.
 - ⁷¹W. H. W. Y. Shih, W. H. W. Y. Shih, S. I. Kim, J. Liu, and I. A. Aksay, “Scaling behavior of the elastic properties of colloidal gels,” *Physical Review A* **42**, 4772–4779 (1990).
 - ⁷²H. Wu and M. Morbidelli, “Model relating structure of colloidal gels to their elastic properties,” *Langmuir* **17**, 1030–1036 (2001).
 - ⁷³A. Zaccone, D. Gentili, H. Wu, M. Morbidelli, and E. Del Gado, “Shear-driven solidification of dilute colloidal suspensions,” *Phys. Rev. Lett.* **106**, 138301 (2011).
 - ⁷⁴M. Wyart and M. E. Cates, “Discontinuous shear thickening without inertia in dense non-brownian suspensions,” *Physical Review Letters* **112** (2014), 10.1103/PhysRevLett.112.098302, arXiv:1311.4099.
 - ⁷⁵B. M. Guy, J. A. Richards, D. J. Hodgson, E. Blanco, and W. C. Poon, “Constraint-Based Approach to Granular Dispersion Rheology,” *Physical Review Letters* **121**, 128001 (2018), arXiv:1807.11356.
 - ⁷⁶J. A. Richards, B. M. Guy, E. Blanco, M. Hermes, G. Poy, and W. C. K. Poon, “The role of friction in the yielding of adhesive non-Brownian suspensions,” *Journal of Rheology* **64**, 405–412 (2020), arXiv:1910.07958.
 - ⁷⁷Y. Wang and R. H. Ewoldt, “New insights on carbon black suspension rheology – anisotropic thixotropy and anti-thixotropy,” arXiv:2202.05772, 1–31 (2022), arXiv:2202.05772.
 - ⁷⁸S. R. Aragón and R. Pecora, “Theory of dynamic light scattering from polydisperse systems,” *The Journal of Chemical Physics* **64**, 2395–2404 (1976).
 - ⁷⁹J. Teixeira, “Small-angle scattering by fractal systems,” *Journal of Applied Crystallography* **21**, 781–785 (1988).
 - ⁸⁰G. Beaucage, “Approximations Leading to a Unified Exponential/Power-Law Approach to Small-Angle Scattering,” *Journal of Applied Crystallography* **28**, 717–728 (1995).
 - ⁸¹G. Beaucage, “Small-Angle Scattering from Polymeric Mass Fractals of Arbitrary Mass-Fractal Dimension,” *Journal of Applied Crystallography* **29**, 134–146 (1996).